

Sand Ripples and Dunes

François Charru,¹ Bruno Andreotti,²
and Philippe Claudin²

¹Institut de Mécanique des Fluides de Toulouse, CNRS-INP-UPS – Université de Toulouse, 31400 Toulouse, France; email: francois.charru@imft.fr

²Laboratoire de Physique et Mécanique des Milieux Hétérogènes, PMMH UMR 7636 ESPCI – CNRS – Université Paris Diderot – Université Pierre et Marie Curie, 75005 Paris, France; email: andreotti@pmmh.espci.fr, claudin@pmmh.espci.fr

Annu. Rev. Fluid Mech. 2013. 45:469–93

First published online as a Review in Advance on October 8, 2012

The *Annual Review of Fluid Mechanics* is online at fluid.annualreviews.org

This article's doi:
10.1146/annurev-fluid-011212-140806

Copyright © 2013 by Annual Reviews.
All rights reserved

Keywords

bed forms, sediment transport, relaxation phenomena, instability, turbulent flow, laminar flow

Abstract

An erodible bed sheared by a fluid flow, gas or liquid, is generally unstable, and bed forms grow. This review discusses the following issues, in light of the recent literature: What are the relevant dynamical mechanisms controlling the emergence of bed forms? Do they form by linear instability or nonlinear processes such as pattern coarsening? What determines their timescales and length scales, so different in air and water? What are the similarities and differences between aeolian and subaqueous patterns? What is the influence of the mode of transport: bed load, saltation, or suspension? Can bed forms emerge under any hydrodynamical regime, laminar and turbulent? Guided by these questions, we propose a unified description of bed-form growth and saturation, emphasizing the hydrodynamical regime in the inner layer and the relaxation phenomena associated with particle transport.

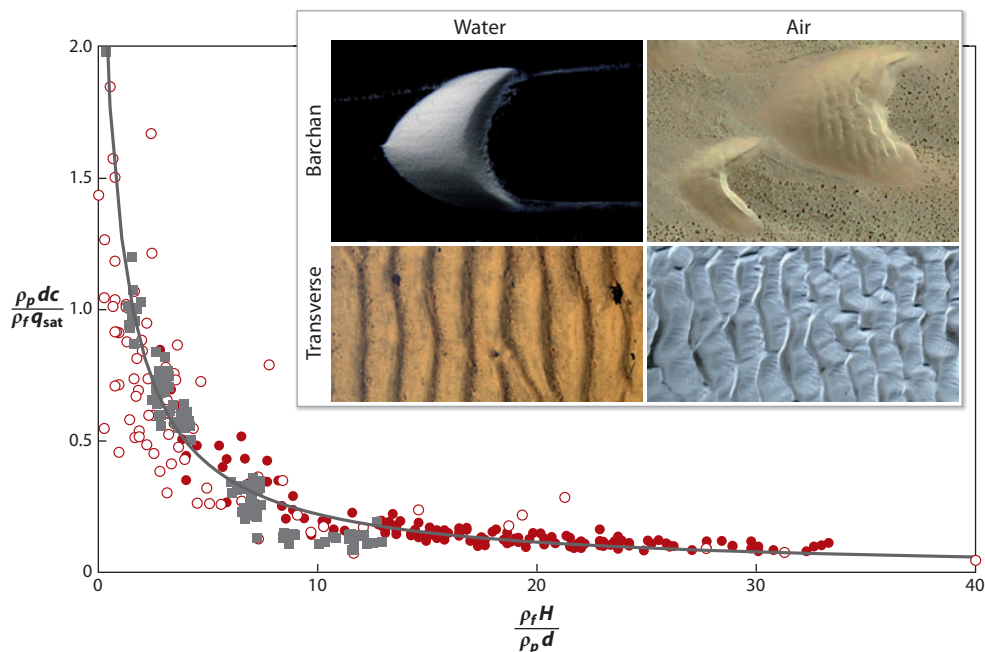


Figure 1

Migration velocity c of dunes as a function of their height H for aeolian barchan dunes (*filled circles*), dunes propagating on the back of large aeolian dunes (*open circles*), and subaqueous barchan dunes (*squares*). The solid line is Bagnold's prediction. (*Inset*) Photographs of barchan (*top*) and transverse (*bottom*) dunes formed under water (*left*) and air (*right*). Note the superimposed bed forms on the back of aeolian dunes.

1. INTRODUCTION

Sand or granular patterns may emerge from an erodible bed sheared by a fluid flow in a wide variety of environments, such as in water channels, rivers, and coastal areas (Best 2005), in deserts on Earth (Bagnold 1941, Pye & Tsoar 1990), and under methane or CO_2 atmospheres on other planets (Bourke et al. 2010), and in hydraulic engineering and industrial pipe flows (Schafflinger et al. 1995, Stevenson et al. 2001). Their size can range from the centimeter scale for subaqueous ripples to 100 m for large river megadunes, from 10 m for the smallest aeolian dunes to 1 km for the largest ones. Mature, finite-height bed forms are typically asymmetric, with an avalanche slip face on their lee side. More generally, the shape of bed forms depends on the symmetries of the fluid forcing or the boundary conditions (Andreotti et al. 2009, Fryberger & Dean 1979). The dynamics of these patterns results from the interaction between the fluid flow and the bed topography through particle transport. For unidirectional flow (**Figure 1**), the fluid accelerates on the windward slope and decelerates on the lee side. Grains are therefore eroded upstream of the crest and deposited downstream. The resulting migrating velocity c is inversely proportional to the dune height H (**Figure 1**), a simple result of great importance that arises from mass conservation (Bagnold 1941).

The wide occurrence of sand patterns has stimulated a large number of studies aiming to increase our understanding. Since the pioneering book of Bagnold (1941), significant progress has been achieved, which has been reviewed, notably, by Engelund & Fredsøe (1982) for ripples and dunes, Blondeaux (2001) for coastal forms, and Seminara (2010) for fluvial sedimentary patterns. Some important unresolved issues, still debated, include the following. What are the relevant dynamical mechanisms controlling the emergence of bed forms? Do they form by linear

Subaqueous ripple:
centimeter-scale
transverse bed form
created by steady
water flow over an
erodible bed

OSCILLATING RIPPLES

The oscillatory motion of a liquid above a granular bed leads to the formation of ripples, as under steady flow (Rousseaux et al. 2004, Sleath 1976). The sand ripples one observes on a beach at low tide are an example: These ripples were formed by the oscillations induced by the surface waves when the beach was covered with shallow water. The mechanism of their formation, related to fluid inertia, is the same as that of ripples under steady flow, with positive phase advance of the shear stress dragging the particles toward crests during each half-period (Blondeaux 1990, Charru & Hinch 2006b). The net particle flux toward crests can also be understood as the result of the mean steady drift flow (steady streaming). Similar structures are also observed on the continental shelf at water depths of 200–300 m, with a wavelength of the order of 1 m. These ripples play an important role in attenuating the wave motion, essentially owing to dissipation in the oscillating boundary layer and vortex detachment from their peaks.

instability or nonlinear processes such as pattern coarsening? What determines their timescales and length scales, so different in air and water? What are the similarities and differences between aeolian and subaqueous patterns (**Figure 1**)? What is the influence of the mode of transport: bed load, saltation, or suspension? Can bed forms emerge under any hydrodynamical regime, laminar and turbulent? The aim of the present review is to propose, based on the recent literature, a unified description of bed-form growth and a hierarchy of the relevant parameters and corresponding regimes. For this purpose, we focus on the canonical situation of transverse bed forms under an unbounded, steady, unidirectional flow. The article is organized as follows. In Section 2, we review the hydrodynamics above an undulated fixed bottom. In Section 3, we discuss the dynamics of sediment transport. Section 4 is devoted to the linear stability analysis of a flat bed and some nonlinear developments. Finally, finite-size effects are discussed in Section 5. Ripples formed under oscillating flow are briefly discussed in the sidebar, Oscillating Ripples.

2. FLUID DYNAMICS OVER A WAVY BOTTOM IN THE UNBOUNDED LIMIT

2.1. Flow Over a Flat Bottom

We begin by considering the flow of a fluid with kinematic viscosity ν and density ρ_f , exerting on a flat bottom a shear stress $\tau_0 = \rho_f u_*^2$, where u_* is the friction velocity. x , y , and z denote the streamwise and spanwise directions and the normal to the bottom, respectively. The bottom comprises grains of characteristic diameter d , located at $z = 0$ (for a precise definition of this location, see, e.g., Raupach et al. 1991). Far enough from the bed, the flow is generally turbulent with logarithmic velocity profile

$$U(z) = \frac{u_*}{\kappa} \ln \left(\frac{z}{z_0} \right), \quad (1)$$

where $\kappa \approx 0.4$ is the von Kármán constant. This “law of the wall” (Raupach et al. 1991) involves a length z_0 , called the hydrodynamical roughness, which is picked up by the matching, which is inherited from a surface layer. For small enough d , the surface layer corresponds to the viscous sublayer, with a thickness that is approximately six times the viscous length $\delta_v = \nu/u_*$ and a linear velocity profile

$$U(z) = (u_*/\delta_v)z. \quad (2)$$

Aeolian ripple:

centimeter-scale bed form created by the impact on a sand bed of saltating grains entrained by the wind; the formation of these ripples, quite different from that of subaqueous ripples, is out of the scope of the present review

Oscillating ripples:

subaqueous ripples created by oscillating flow

Table 1 Typical flow conditions and length scales for a sand bed under oil ($\nu = 10^{-5} \text{ m}^2 \text{ s}^{-1}$), water ($\nu = 10^{-6} \text{ m}^2 \text{ s}^{-1}$), and air ($\nu = 15 \times 10^{-6} \text{ m}^2 \text{ s}^{-1}$)

Fluid flow	u_* (m s ⁻¹)	d (mm)	d/δ_v	λ (m)	δ_i (mm)	δ_i/δ_t	$kz_0 \times 10^3$	Θ	L_{sat}/d
Oil	0.02	0.1	0.2	0.1	1	5	3 (TR)	0.25	≈ 20
Water	0.02	0.2	4	0.1	1.4	4	0.3 (TR)	0.12	≈ 10
Air	0.4	0.2	5	50	500	50	0.03 (TU)	0.05	$\approx 10^4$

Definitions: friction velocity u_* , grain diameter d , particle Reynolds number d/δ_v , typical wavelength λ , inner layer thickness δ_i , scale separation δ_i/δ_t (TR, transitional regime; TU, turbulent regime), kz_0 , Shields number θ , and L_{sat}/d .

The flow is said to be dynamically smooth, and the hydrodynamical roughness is given by $z_0 \approx 0.11 \delta_v$. A good estimate of the full velocity profile can be obtained from the momentum equation $u_*^2 = [\nu + \ell^2 U'(z)]U'(z)$ with an exponential damping of the Prandtl mixing length as the bed is approached,

$$\ell = \kappa z[1 - \exp(-z/\alpha\delta_v)], \quad (3)$$

where $\alpha \approx 25$ is the van Driest number (Pope 2000). For d larger than, e.g., $10\delta_v$, the viscous sublayer is no longer relevant, and the flow is said to be hydrodynamically rough. Measurements then give, for fixed grains, $z_0 \approx 0.03\text{--}0.1d$ (Andreotti 2004, Bagnold 1941, Kamphuis 1974). A usual, yet phenomenological, description introduces the mixing length (Ayotte et al. 1994, Colombini 2004, Fourrière et al. 2010, Richards 1980)

$$\ell = \kappa(z + z_0). \quad (4)$$

The existence of a layer of moving grains at the bed surface may increase the roughness z_0 (see Section 3).

2.2. Linear Response of the Flow to a Wavy Wall

In this section, we discuss the linear response of the flow to a wavy wall, distinguishing the laminar, intermediate, and turbulent regimes.

2.2.1. Structure of the flow disturbance and bottom shear stress. Now let us consider a disturbed bottom in the simplest situation of small-amplitude two-dimensional waves, $\zeta = \zeta_0 \cos kx$. Typical values of the parameters are given in **Table 1**. For small wave slope, typically $k\zeta_0 < 0.1$ ($2\zeta_0/\lambda < 0.03$), the flow disturbance is sinusoidal and proportional to $k\zeta_0$; i.e., the response is linear. The measurements displayed in **Figure 2** show such a linear response of the shear stress τ_b and the presence of higher harmonics for larger slope. We note, in particular, the phase advance with respect to the bottom. The linear stability problem amounts to the determination, for small slope, of

$$\tau_b = \frac{1}{2}(\hat{\tau}e^{ikx} + \hat{\tau}^*e^{-ikx}), \quad \hat{\tau} = \tau_0(\mathcal{A} + i\mathcal{B})k\zeta_0, \quad (5)$$

where \mathcal{A} and \mathcal{B} are the components in phase and in quadrature with the bottom, respectively. This subsection focuses on the unbounded limit, $kD \gg 1$, where the vertical extent D of the flow is larger than the penetration depth $\approx 2\pi/k$ of the flow disturbance, so that \mathcal{A} and \mathcal{B} depend on the single parameter kz_0 .

Figure 3 shows measurements as well as theoretical predictions of $\mathcal{A}(kz_0)$ and $\mathcal{B}(kz_0)$. The reference curve (Hanratty's model) is based on the Reynolds-averaged Navier-Stokes (RANS)

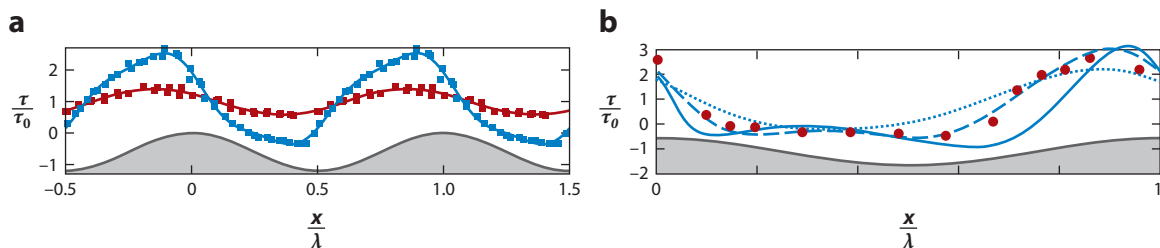


Figure 2

Bottom shear stress τ/τ_0 on a smooth sinusoidal bottom (gray line). (a) Measurements for $2\xi_0/\lambda = 0.0125$ (red squares) and 0.05 (blue squares) (Zilker et al. 1977) and the best fit with three harmonics (solid lines). (b) Measurements for $2\xi_0/\lambda = 0.2$ [circles; Buckles et al. 1984] and large-eddy simulation for $2\xi_0/\lambda = 0.0125$ (dotted line), 0.1 (dashed line), and 0.2 (solid line) (Henn & Sykes 1999).

equations and the mixing length (Equation 3). For a given base flow, four hydrodynamical regimes can be identified, controlled by kz_0 , which are detailed below.

2.2.2. Viscous and inertial laminar regimes. At large wave numbers, the flow disturbance is confined within the viscous sublayer in which the velocity profile (Equation 2) is linear. The problem can therefore be solved by neglecting the turbulent fluctuations (Benjamin 1959, Charru & Hinch 2000, Valance & Langlois 2005). **Figure 3a,b** shows that the corresponding \mathcal{A} and \mathcal{B} (yellow curve) match, in effect, for $k\delta_v \gtrsim 10^{-2}$, the calculation including the Reynolds stresses (red curve). The flow disturbance has a two-layered structure (**Figure 3c**): an outer layer (green) dominated by inertia and an inner layer (orange) dominated by viscosity, in which the flow is driven by the pressure gradient inherited from the outer layer. The thickness δ_i of the inner layer can be defined from the balance of longitudinal advection [$\sim k(u_*^2/\nu)\delta_i$] and transverse viscous diffusion ($\sim \nu/\delta_i^2$), giving

$$\delta_i \sim (\nu^2/ku_*^2)^{1/3} = (\delta_v^2/k)^{1/3}. \quad (6)$$

δ_i also represents the penetration depth of vorticity disturbances so that the flow disturbance in the outer layer is potential. Asymptotic expressions of \mathcal{A} and \mathcal{B} have been derived in the viscous and inertial regimes by Benjamin (1959) and Charru & Hinch (2000):

$$\mathcal{A} + i\mathcal{B} = 2 + i\frac{1}{2}(k\delta_i)^{-3} = 2 + i\frac{1}{2}(k\delta_v)^{-2} \quad (k\delta_i \gg 1), \quad (7)$$

$$\mathcal{A} + i\mathcal{B} = \gamma_L(k\delta_i)^{-1} e^{i\pi/6} = \gamma_L(k\delta_v)^{-2/3} e^{i\pi/6} \quad (k\delta_i \ll 1), \quad (8)$$

where $\gamma_L \approx 1.06$. **Figure 3** shows that these expressions (orange and green dashed lines) are close to the exact calculation (yellow curve).

2.2.3. Turbulent regime. For small wave numbers, the flow disturbance extends far beyond the surface layer so that Reynolds stresses cannot be neglected. **Figure 3** shows that \mathcal{A} and \mathcal{B} depend slowly on kz_0 , logarithmically, as expected. The asymptotic analysis was first tackled by Jackson & Hunt (1975) and then improved in several ways, notably by Sykes (1980) (reviewed in Belcher & Hunt 1998). This analysis assumes that the surface layer—which selects z_0 , viscous or not—has a thickness much smaller than δ_i and is valid for both the hydrodynamically rough and smooth regimes. In the long wave limit, $kz_0 \ll 1$, in which the inner layer thickness δ_i is much smaller than the wavelength [i.e., when $\ln(\delta_i/z_0) \gg 1$], the two-layer structure is recovered as illustrated in the far left of **Figure 3c**: an outer layer in which the disturbed flow is dominated by inertia (green) and an inner layer dominated by Reynolds stresses (blue). From the balance of

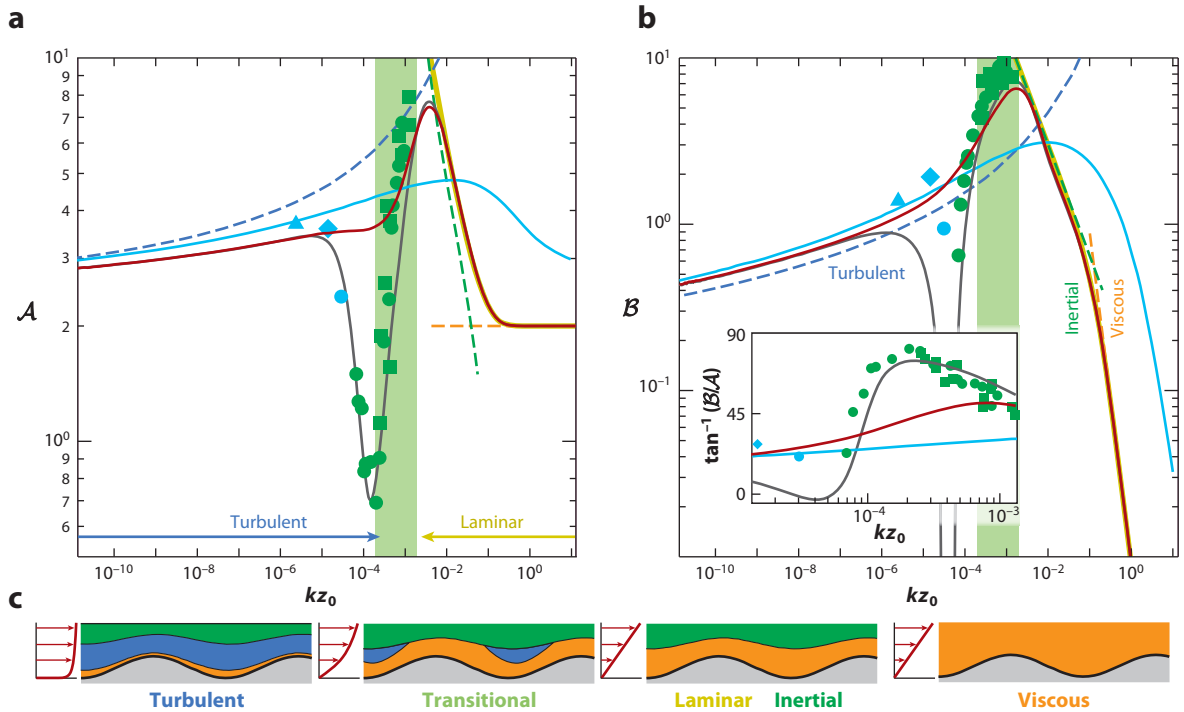


Figure 3

Shear-stress components (a) in-phase A and (b) in-quadrature B as a function of the wave number kz_0 . (Inset) Phase shift $\tan^{-1}(B/A)$ in degrees. The solid lines represent full calculations, and the dashed lines are asymptotic calculations: smooth closure (Equation 3) (solid red line), Hanratty's model (solid gray line), rough closure (Equation 4) (solid blue line), laminar Couette flow (solid yellow line), Equation 10 (dashed blue line), Equation 7 (dashed orange line), and Equation 8 (dashed green line). The green region is the transition between the laminar and turbulent regimes ($10^{-5} < kz_0 < 10^{-3}$). Data are taken from electrochemical measurements (green circles and squares) (Frederick & Hanratty 1988 and Zilker et al. 1977, respectively), from velocity measurements on a 40-m-long protodune [blue triangle (Claudin et al. 2012)], and from flumes [blue diamonds (Poggi et al. 2007) and blue circles (Finnigan et al. 1990)]. (c) Schematics of the layered structure of the disturbed flow in the different regimes.

longitudinal advection and the turbulent stresses as given by the Prandtl mixing-layer theory, the thickness δ_i of the inner layer is given by the implicit relation

$$\frac{\delta_i}{\lambda/4} \ln(\delta_i/z_0) = 2\kappa^2. \quad (9)$$

(Another expression has been proposed that involves the square of the logarithm and provides smaller δ_i .) From the matching of the outer and inner flows, we find the shear-stress components A and B to be

$$A + iB = 2 \frac{U^2(\delta_m)}{U^2(\delta_i)} \left[1 + \frac{1 + 2 \ln(\pi/2) + 4\gamma_E + i\pi}{\ln(\delta_i/z_0)} \right], \quad (10)$$


where U is the logarithmic velocity profile (Equation 1), $\gamma_E \simeq 0.577$ is Euler's constant, and $\delta_m = (\lambda/4z_0) \ln^{-1/2}(\lambda/4z_0)$ (Hunt et al. 1988, Kroy et al. 2002, Weng et al. 1991). **Figure 3a,b** shows that these asymptotic expressions (curves from Equation 10, dashed blue lines) are valid for $kz_0 \lesssim 10^{-5}$.

The bottom shear stress has not been measured in the turbulent regime, so only indirect determinations of A and B can be obtained from velocity measurements in the inner layer, assuming that the log velocity profile holds locally. As shown in **Figure 3**, they reasonably match the

predictions (blue symbols). Moreover, these velocity measurements confirm the linear increase of the mixing length with the distance to the bottom (Poggi et al. 2007). As shown numerically by Ayotte et al. (1994), the predictions for the inner layer (\mathcal{A} and \mathcal{B} , in particular) are robust to changes in the turbulence closure scheme: mixing-length schemes (Colombini 2004, Fourrière et al. 2010, Mason & King 1985), models with equations for the turbulent kinetic energy, and true second-order closures (Finnigan et al. 1990, Weng et al. 1991). Because the timescale over which turbulent fluctuations adapt to the shear rate scales as δ_i/u_* in the inner layer, out-of-equilibrium turbulence effects vanish as $\ln^{-1}(\delta_i/z_0)$.

Conversely, in the outer layer, the flow disturbance depends significantly on the closure law, especially Reynolds stresses. Second-order closures have revealed the influence of the lag between the production and dissipation of turbulent fluctuations, related by Finnigan et al. (1990) to streamline curvature effects. This results in a phase lag of the shear stress with respect to the topography (van Boxel et al. 1999, Walker & Nickling 2003, Weng et al. 1991, Wiggs et al. 1996), which contrasts with the phase advance in the inner layer. Another important effect in the outer layer is the rapid distortion of turbulence by the mean shear, which results in Reynolds stress anisotropy (Ayotte et al. 1994, Finnigan et al. 1990).

2.2.4. Transitional regime. Most of the measurements of \mathcal{A} and \mathcal{B} reported in **Figure 3** were obtained by Zilker et al. (1977) and Frederick & Hanratty (1988) (green points), and fall in the range $10^{-5} < kz_0 < 10^{-3}$ (green regions in all the figures). They clearly disagree with the calculations performed with a simple mixing-length closure (red curve). For this range of kz_0 , the perturbation partly penetrates the turbulent region so that neither viscosity effects nor turbulent fluctuations can be neglected. On the upstream face of a bump at which the flow is accelerated, the more negative streamwise pressure gradient tends to damp the turbulent fluctuations so that the viscous sublayer thickens, whereas the opposite is true on the lee side. This results in a periodic transition from the viscous to the turbulent inner layer (see **Figure 3c**). Following Abrams & Hanratty (1985) and Frederick & Hanratty (1988), one can account for this effect by a dependence of the van Driest number α in Equation 3 on the pressure gradient, with a space lag of the order of $\alpha^3\delta_v$ (from the classical argument for the thickening of a boundary layer) (see the **Supplemental Appendix**; follow the **Supplemental Material link** from the Annual Reviews home page at <http://www.annualreviews.org>). The prediction of this model, Hanratty's model, is shown in **Figure 3a,b** (gray solid line) and nicely fits the measurements. The modulation effect is resonant for wave numbers $k\delta_v \approx 2\pi/\alpha^3 \approx 10^{-3}$, hence the large effect on \mathcal{A} and \mathcal{B} in the vicinity of this value. Although this model provides a convenient parameterization, a true understanding of the interplay between a wavy bottom and the modulation of the viscous sublayer remains to be achieved.

 **Supplemental Material**

2.2.5. Physical mechanism of the phase lag between shear stress and topography. The most important result of the above analyses is that both \mathcal{A} and \mathcal{B} are positive so that the shear-stress maximum is generically located upstream of the crest. The physical mechanism of this phase advance can be understood as follows. In the outer layer in which the flow perturbation is essentially inviscid and potential (unlike the base state), the flow accelerates upstream of crests and decelerates downstream, with opposite variation for the pressure (the Bernoulli effect). This pressure also drives the flow in the inner layer, but there the bottom friction opposes the velocity variations. Because of fluid inertia, the variation of the shear stress must drive that of the fluid velocity, hence the positive phase advance. For a more quantitative discussion in the laminar regime, readers are referred to Charru & Hinch (2000). As discussed in the following sections, this phase advance is responsible for the instability of an erodible bed.

2.3. Beyond the Linear Response

For a sinusoidal bottom with slope $k\zeta_0 \simeq 0.1$ (Kuzan et al. 1989), hydrodynamical nonlinear effects are no longer negligible. Harmonics grow, and the phase advance of the shear stress decreases (**Figure 2**) (Richards & Taylor 1981). Most numerical simulations (RANS, large-eddy simulations, direct numerical simulations) and experiments in water have been performed in the transitional regime (Buckles et al. 1984, Cherukat et al. 1998, de Angelis et al. 1997, Frederick & Hanratty 1988, Henn & Sykes 1999, Zilker & Hanratty 1979), for which the linear regime itself is not well understood, as discussed above. In the simpler turbulent regime, the qualitative aspects of the nonlinear hydrodynamical response have been elucidated from field observations, wind-tunnel experiments, and numerical simulations over both the sinusoidal bottom and isolated bumps (Buckles et al. 1984, Finnigan et al. 1990, Gong & Ibbetson 1989, Gong et al. 1996, Salvetti et al. 2001, Taylor et al. 1987, Yue et al. 2006, Zilker & Hanratty 1979). The linear asymptotic theory of Hunt et al. (1988) still predicts the dominant features of the flow (Belcher & Hunt 1998). On the upstream side of bumps, vertical profiles of the speedup remain correctly described. In contrast, on the lee side, the Prandtl mixing-length model fails to describe the flow, and more elaborate closures schemes are necessary there (Ross et al. 2004, van Boxel et al. 1999).

On erodible beds, the initial sinusoidal topography also deforms and becomes asymmetric, whereas the height-to-length ratio tends toward approximately 1/15 for mature subaqueous ripples and aeolian dunes (Baddock et al. 2007, Parteli et al. 2006). An avalanche slip face develops on the lee side, from which the mean flow separates and a recirculation bubble forms. From the coupling between hydrodynamics and erosion deposition, the instability saturates, and the sand flux and elevation profiles vary in phase.

From a theoretical point of view, the main difficulty is the quantitative description of flow separation, which, for a sinusoidal bottom, occurs for $k\zeta_0 \gtrsim 0.3$ (Buckles et al. 1984, Finnigan et al. 1990, Henn & Sykes 1999, Zilker & Hanratty 1979). Aside from studies based on the triple-deck theory (Lagrée 2003), heuristic linear calculations have been proposed of the turbulent flow above a fictive obstacle comprising the true obstacle prolonged by the separation streamline (Finnigan et al. 1990, Jensen & Zeman 1985). However, separation is associated with the development of complex turbulent structures. An inflection point appears in the mean velocity profile, corresponding to the formation of a free shear layer. Spanwise vortices develop because of Kelvin-Helmholtz instability, which vortices then impinge on the bottom near the reattachment point. Downstream of this point, very large velocity gradients take place close to the wall, associated with large shear stress (**Figure 2b**) and followed by the formation of longitudinal streaks and hairpin vortices. When the reattachment length is larger than the wavelength, the free shear layer spreads and rises, and a new free shear layer is created downstream of the next crest, resulting in large production of turbulence and strong mixing of momentum. Large-scale streamwise vortices emerge with spanwise wavelength scaling on the streamwise wavelength of the bottom (Hudson et al. 1996, Kruse et al. 2003).

A complete description of the nonlinear response is definitely beyond the present review and remains a major challenging issue. A promising direction is weakly nonlinear analysis, following studies in the laminar regime (Bordner 1978, Caponi et al. 1982, Valance 2011) and turbulent regime (Andreotti et al. 2009, Colombini & Stocchino 2008) (the coupling with the neutral mode $k = 0$, arising from Equation 11, has not been included in the analysis yet). Another possible direction is the development of the triple-deck theory for turbulent flow.

3. THE SCALES OF PARTICLE TRANSPORT

The observed modes of transport can be associated with the different forces acting on the particles. When the hydrodynamic forces exceed some threshold value related to the bed disorder at the

particle scale [a fraction of the immersed weight $(\rho_p - \rho_f)gd^3$], the particles at the bed surface are set into motion. When the particles and the fluid have comparable densities (typically sand grains in water), the moving particles roll and slide on each other within a thin layer, of a few diameters thick, and this mode of transport is called bed load. Lubrication forces are responsible for the dissipation. Conversely, for large ratio ρ_p/ρ_f (typically sand grains in air), the grains experience large jumps, and the transport mode is called saltation. Dissipation mainly results from the collisions of the moving particles with the bed. Finally, when the fluid velocity fluctuations, of magnitude u_* , become comparable with the settling velocity V_{fall} , of the order of $\sqrt{(\rho_p/\rho_f - 1)gd}$, grains are dispersed throughout the whole fluid layer, and this mode of transport is called suspension.

Saturation length: distance needed for nonequilibrium particle flux to relax toward its saturated value

3.1. What Is the Hydrodynamic Parameter Controlling Transport?

The spatiotemporal evolution of the bed profile $\zeta(x, t)$, which is our primary interest, is related to the particle flux per unit width, $q(x, t)$, through the mass conservation equation

$$\phi_b \frac{\partial \zeta}{\partial t} = -\frac{\partial q}{\partial x}, \quad (11)$$

where $\phi_b \approx 0.6$ is the volume fraction of the bed. Transport models aim at relating the flux q to the fluid flow. They are usually calibrated in homogeneous and steady situations controlled by a single hydrodynamic parameter: the bed shear stress τ , or equivalently the shear velocity u_* . The resulting particle transport is characterized by the so-called saturated flux $q_{\text{sat}}(\tau)$. Because of the trapping of the particles by gravity, q_{sat} vanishes below a threshold value $\tau_{\text{th}} = \rho_f u_{\text{th}}^2 \sim (\rho_p - \rho_f)gd$, which is sensitive to the geometrical disorder of the granular bed (Charru et al. 2004). Introducing the Shields number $\Theta = \tau/[(\rho_p - \rho_f)gd]$, dimensional analysis gives the general form of the transport law as

$$q_{\text{sat}} = u_s d \mathcal{Q}(\Theta), \quad (12)$$

where u_s is a characteristic velocity. The usual choice for u_s is the characteristic settling velocity $\sqrt{(\rho_p/\rho_f - 1)gd}$, but models based on the balance of horizontal momentum rather bring $u_s = u_{\text{th}}$. The dimensionless function \mathcal{Q} depends, in addition to Θ , on the density ratio ρ_p/ρ_f , which controls, in particular, the transition from bed load to saltation, and on the settling Reynolds number $Re_s = V_{\text{fall}}d/\nu$ (or equivalently the threshold Reynolds number $Re_{\text{th}} = u_{\text{th}}d/\nu$), which controls the hydrodynamical regime at the grain scale.

When the bed topography is modulated by bed forms, the shear stress and particle flux are no longer uniform. This raises two issues. First, does the saturated transport law still hold? Early investigations have assumed local saturation of the sediment transport, with the local flux $q = q_{\text{sat}}(\tau)$ controlled by the local shear stress τ . However, there is experimental evidence that transport does not adapt instantaneously to a spatial change of the shear stress (Anderson & Haff 1988). As an illustration, **Figure 4a** displays the spatial relaxation of the flux toward saturation downstream of the transition between a nonerodible bottom ($x < 0$) and an erodible bed ($x > 0$), in the aeolian case, whereas **Figure 4b** displays similar results for suspension. However, over bed forms, the transport is never far from its saturated state, so it can be described by a first-order linear relaxation in space and time:

$$T_{\text{sat}} \frac{\partial q}{\partial t} + L_{\text{sat}} \frac{\partial q}{\partial x} = q_{\text{sat}} - q, \quad (13)$$

where L_{sat} and T_{sat} are the saturation length and times (Andreotti et al. 2002, Charru 2006, Claudin et al. 2011, Narteau et al. 2009, Parker 1975, Sauermann et al. 2001). Regarding ripples and dunes, the first term of this equation can be safely neglected, as T_{sat} is usually much smaller (~ 1 s) than

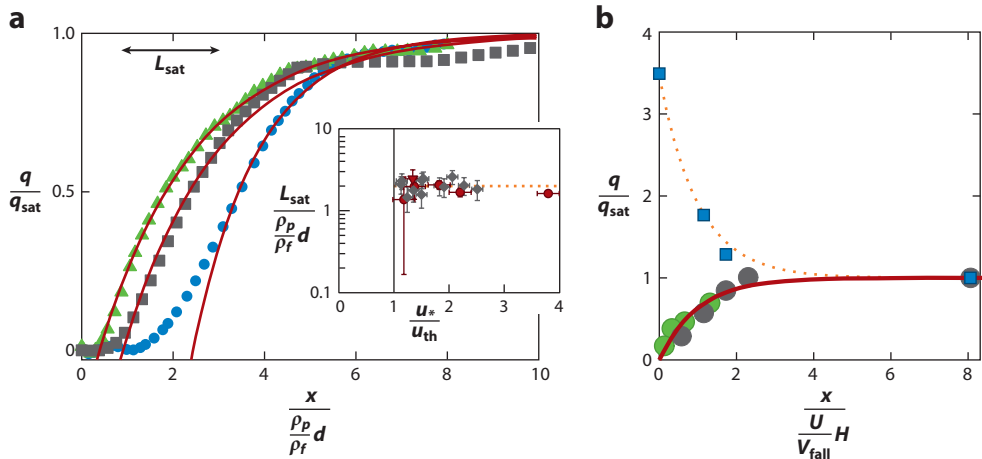


Figure 4

Relaxation of the sediment flux q toward q_{sat} : (a) aeolian transport and (b) suspension. (a) The wind erodes a sand patch starting at $x/L_{\text{drag}} = 0$ with drag length $L_{\text{drag}} = \frac{\rho_p}{\rho_f} d$: $u_*/u_{\text{th}} \simeq 1.8$ (triangles), $u_*/u_{\text{th}} \simeq 1.5$ (squares), and $u_*/u_{\text{th}} \simeq 1.2$ (circles). The red lines represent the best exponential fits $q/q_{\text{sat}} = 1 - \exp(-x/L_{\text{sat}})$ (Andreotti et al. 2010). (Inset) $L_{\text{sat}}/L_{\text{drag}}$ as a function of u_*/u_{th} , showing (gray symbols) direct measurements from wind-tunnel experiments and (red symbols) indirect estimates from an analysis of initial dune wavelengths (field data). The dotted line represents $L_{\text{sat}} = 2(\rho_p/\rho_f)d \approx 0.8$ m. (b) Similar measurements for particles transported in suspension, with the distance x rescaled by the deposition length $L_{\text{dep}} = (U/V_{\text{fall}})D$, for net erosion [green circles (van Rijn 1986) and gray circles (Ashida & Okabe 1982)] and net deposition [blue squares (Ashida & Okabe 1982)], along with exponential fits (solid and dotted lines).

the bed-form growth time ($\sim 10^2$ s for subaqueous ripples and $\sim 10^5$ s for aeolian dunes). This separation justifies the simplifying assumption that the fluid flow can be computed as if the bed were fixed. The physical significance of L_{sat} is discussed below.

Second, at which vertical location should the shear stress be evaluated? As discussed in the previous section, τ can exhibit large vertical gradients in the outer layer, so the question deserves attention. The usual approach uses $\tau[z = \zeta(x, t)]$, which is a rigorous approximation when the transport layer, of thickness δ_t , is much thinner than the inner layer (typically, $\delta_t \approx d \approx 10^{-1} \delta_i$ in water close to threshold and $\delta_t \approx \frac{\rho_p}{\rho_f} d \approx 10^{-2} \delta_i$ in air). Colombini (2004) proposed an alternative approach, which evaluates the shear stress at the distance $z = \zeta(x, t) + \delta_t$. Although appealing, this approach considers that the transport layer behaves as a pure fluid, which is clearly not the case. Further investigation is needed, accounting for the two-phase nature of the transport layer and the shear-stress gradient, in which the latter is embedded.

3.2. Linear Response of the Saturated Flux

Equation 13 describes the linear response of the flux q to a change of the saturated flux q_{sat} . To complete the description of transport on bed forms, one needs the linear response of q_{sat} to a small change $\delta\tau$ of the shear stress τ and to a small change $s = \partial_x \zeta$ of the local bed slope from the horizontal direction. The response to $\delta\tau$ can be written $(\phi_b Q/\tau)\delta\tau$, where Q is the susceptibility with respect to the shear stress:

$$Q = \frac{\tau}{\phi_b} \left. \frac{\partial q_{\text{sat}}}{\partial \tau} \right|_{\tau}. \quad (14)$$

Saturated flux:

volume of particles transported per unit time and width, in equilibrium with the shear stress exerted by the fluid flow

As gravity tends to entrain particles downward, a slope induces an additional contribution to the flux $-SQ_s$, where S is the susceptibility with respect to the slope:

$$S = -\frac{1}{Q} \left. \frac{\partial q_{\text{sat}}}{\partial s} \right|_{s=0}. \quad (15)$$

For $q \propto (\tau - \tau_{\text{th}})^n$ and with the assumption that the slope effect can be embedded in the change of the transport threshold, $\delta\tau_{\text{th}}/\tau_{\text{th}} = s/\mu$, where μ is an effective friction coefficient, one obtains $S = \frac{1}{\mu} \tau_{\text{th}}/\tau$. Experiments give $\mu \simeq \tan 37^\circ$ in tilted wind tunnels (Iversen & Rasmussen 1999), and for bed load in water, $\mu \simeq \tan 35^\circ$ (Dey 2003, Fernandez Luque & van Beek 1976) or $\mu \simeq \tan 65^\circ$ (Loiseleux et al. 2005), which are values consistent with the avalanche angle. Finally, S typically decreases from ≈ 1.6 at the transport threshold to zero at large flow velocity.

3.3. What Are the Dynamical Mechanisms Controlling Sediment Transport?

The scaling laws followed by q_{sat} , L_{sat} , and z_0 depend on the dynamical mechanisms controlling transport. We briefly review the results obtained for the three modes of transport.

3.3.1. Bed load in water. The physical explanation proposed by Bagnold (1956) for the equilibrium bed-load transport in the turbulent case is as follows. The moving particles are confined within a thin transport layer of thickness $\delta_t \simeq d$ and have a mean velocity $u_p \propto u_* - \beta u_{\text{th}}$, where $\beta < 1$ characterizes the effective bed friction. Across the transport layer, the fluid transmits momentum to the particles in proportion to the number n of mobile grains per unit surface. The equilibrium transport corresponds to the fluid shear stress being reduced to the threshold at the fixed bed, which leads to $n \propto u_*^2 - u_{\text{th}}^2$. As the flux is $q = nu_p$, one obtains $Q \sim (\Theta - \Theta_{\text{th}})(\sqrt{\Theta} - \beta\sqrt{\Theta_{\text{th}}})$. The scaling of the sediment flux with the third power of the shear velocity, for large $\Theta/\Theta_{\text{th}}$, has been recovered in most experiments (Bagnold 1956). For viscous bed load, similar arguments give $Q \propto \Theta^3$ (Bagnold 1956, Charru & Mouilleron-Arnould 2002, Leighton & Acrivos 1986, Mouilleron et al. 2009, Ouriemi et al. 2009), whereas erosion-deposition models for a monolayer of particles, close to threshold, lead to $Q \propto \Theta^2$ (Charru & Hinch 2006a).

The saturation transient may be controlled by two mechanisms: the erosion or deposition of particles (related to the relaxation of n) and particle inertia (relaxation of u_p). For bed load, Charru & Hinch (2006a) proposed that erosion and deposition are the limiting processes, which leads to the saturation length

$$L_{\text{sat}} \propto \frac{U}{V_{\text{fall}}}, \quad (16)$$

where U is the fluid velocity at the particle scale, and d/V_{fall} is the typical time needed for one particle to settle. Therefore, L_{sat} scales on a deposition length (Lajeunesse et al. 2010). However, L_{sat} has not been measured directly for bed load, unlike for saltation and suspension.

As mentioned in the previous section, bed-load transport may change the hydrodynamical roughness z_0 seen from the inner layer. The measurements collected by van Rijn (1982) show $z_0 = 1 - 10d$, which is significantly larger than for a fixed bed; Richards (1980) used the empirical result that z_0/d increases linearly with Θ . A thorough assessment of these laws remains to be performed. Moreover, in the transitional regime, transport may affect the modulation of the viscous sublayer.

3.3.2. Saltation in air. The stress balance still holds for saltation, and the scaling of n is the same as above (Owen 1964). However, the particle motion takes place over a much thicker layer, $\delta_t \simeq (\rho_p/\rho_f)d \gg d$, in which, contrary to bed load, the wind velocity is strongly reduced because

of the large particle inertia (Andreotti 2004, Ungar & Haff 1987). The entrainment of new grains mostly results from collisions. The balance between erosion and deposition implies that the mean grain velocity u_p is a constant, scaling with u_{th} . The resulting scaling law $Q \sim (\Theta - \Theta_{th})$ is in agreement with wind-tunnel experiments (Creyssels et al. 2009, Iversen & Rasmussen 1999) but contrasts with the initial proposition of Bagnold (1941).

The saturation transient is limited by particle inertia, so the saturation length L_{sat} scales with the length needed for one grain to be accelerated up to the wind velocity (Andreotti et al. 2010, Hersen et al. 2002):

$$L_{sat} \propto \frac{\rho_p}{\rho_f} d. \quad (17)$$

L_{sat} is therefore independent of u_* and is of the order of 1 m, as confirmed by direct measurements (Figure 4a). Note that the initial exponential increase of the sand flux seen in the figure for $q \ll q_{sat}$ results from erosion and takes place over a distance decreasing as u_*^{-2} (Sauermaun et al. 2001).

Experiments (Iversen & Rasmussen 1999) and models (Andreotti 2004, Durán et al. 2011) agree on the large increase of the hydrodynamical roughness z_0 with the density of mobile grains, and therefore with u_* . It provides a direct proof of the strong negative feedback, inside the transport layer, of the particles on the fluid velocity.

3.3.3. Suspension. In the suspension regime ($u_* \gtrsim V_{fall}$), particles diffuse over the whole water depth D , and the particle flux results from the balance between the upward diffusion and sedimentation. Experiments (Ashida & Okabe 1982, Jobson & Sayre 1970, van Rijn 1986) and theoretical analysis (Claudin et al. 2011) have shown that the saturation length then scales as

$$L_{sat} \propto \frac{U}{V_{fall}} D, \quad (18)$$

i.e., on a deposition length based on the depth-averaged flow velocity U and the settling time D/V_{fall} (Figure 4b). This law is the same as for bed load, except that the length over which the grains settle now scales with the flow depth D rather than the grain diameter. As $D/d \gg 1$, L_{sat} can be very large: several meters in flume experiments and hundreds of meters in natural rivers.

4. STABILITY ANALYSIS OF A FLAT ERODIBLE BED

We now address the question of the instability of an erodible bottom by combining the previous analyses of the fluid flow (Section 2) and particle transport (Section 3). The instability mechanism is shown to arise from the hydrodynamics, for both subaqueous ripples and aeolian dunes, whereas gravity and sediment transport are stabilizing. Unbounded flow is still considered here as the reference case.

4.1. Dispersion Relation

As clearly recognized by Kennedy (1963, 1969), a crucial feature at the origin of the growth of a sinusoidal disturbance of an erodible bed is the phase lead of the perturbation τ_b of the bed shear stress, as given by Equation 5. We let $\zeta(x, t) = \zeta_0 e^{\sigma t} \cos(kx - \omega t)$ be the slowly varying bed disturbance. The component of τ_b in quadrature with $\zeta(x, t)$ (proportional to $\mathcal{B} > 0$) drags the particles from troughs to crests, amplifying the initial bed disturbance (positive growth rate σ), whereas the in-phase component (proportional to $\mathcal{A} > 0$) is responsible for the downstream

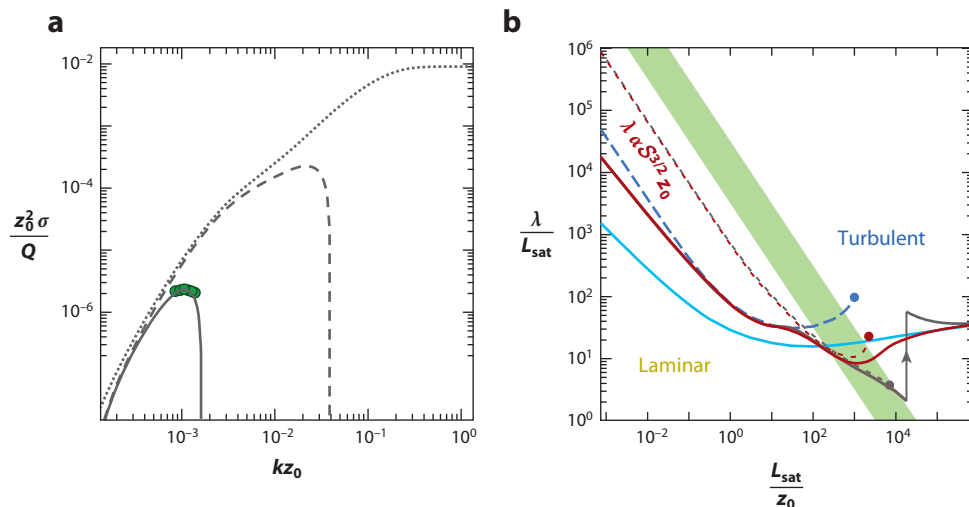


Figure 5

(a) Growth rate σ as a function of wave number kz_0 from Hanratty's model for $L_{\text{sat}} = 0$ and $S = 0$ (dotted line); $L_{\text{sat}} = 0$ and $S = 1.0$ (dashed line); and $L_{\text{sat}} = 90 \delta_v = 36 d$ and $S = 1.0$ (solid line), with these last values chosen to fit measurements (green circles) from Betat et al. (1999). (b) The most unstable wavelength λ rescaled by L_{sat} computed for $S = 0$ (solid lines) and $S = 1.6$ (dashed lines). When $S > B(kz_0)$ for all wave numbers, the flat bed is stable (at the right of the dots ending the dashed lines). Color coding is as follows: smooth closure (Equation 3) (solid red line), Hanratty's model (solid gray line), rough closure (Equation 4) (solid blue line), and Equation 10 (dashed blue line). The green region is the transition between the laminar and turbulent regimes ($10^{-5} < kz_0 < 10^{-3}$).

migration of the disturbance, with a phase velocity $c = \omega/k$. We discuss here the dispersion relation, i.e., the dependence of σ and c on the wave number k .

4.1.1. Stabilizing effects ignored. We first ignore the stabilizing slope effect ($S = 0$) and consider that the particle transport q is at local equilibrium with the shear stress ($L_{\text{sat}} = 0$). Then, as $q = q_{\text{sat}}(\tau)$, the amplitude of the flux disturbance is $\hat{q} = \phi_b Q(A + iB)k\zeta$, with Q defined by Equation 14. The bed evolution is governed by the particle mass conservation equation (Equation 11), and the dispersion relation follows as

$$\sigma = B(kz_0)Qk^2, \quad c = A(kz_0)Qk. \quad (19)$$

Because fluid inertia imposes $B > 0$ for any wave number (Figure 3b), all wave numbers are amplified (Figure 5a). Some stabilizing processes must be at work to get some most amplified wave numbers.

4.1.2. Slope effect. With the introduction of the slope effect, \hat{q}_{sat} becomes

$$\hat{q}_{\text{sat}} = \phi_b Q\{A(kz_0) + i[B(kz_0) - S]\}k\zeta. \quad (20)$$

The additional S term does not provide any new length scale but reduces the growth rate from QBk^2 to $Q(B - S)k^2$. As Bk^2 tends to the constant value $\frac{1}{2}\delta_v^{-2}$ at large k (Section 2), the slope effect stabilizes short waves: Instability is suppressed beyond some cutoff wave number (Figure 5a) (Fredsoe 1974). The slope effect is expected to be significant close to the transport threshold Θ_{th} and become negligible further away as S decreases with increasing shear stress (Section 3).

4.1.3. Transport relaxation. For spatially varying shear stress, the adjustment of the particle flux is not instantaneous but takes place over some relaxation length L_{sat} (Section 3). According to Equation 13, the amplitudes of the actual and saturated flux disturbances, \hat{q} and \hat{q}_{sat} , are then related by $(1 + ikL_{\text{sat}})\hat{q} = \hat{q}_{\text{sat}}$ so that the growth rate and wave velocity become

$$\sigma = Qk^2 \frac{(\mathcal{B} - \mathcal{S}) - AkL_{\text{sat}}}{1 + (kL_{\text{sat}})^2}, \quad c = Qk \frac{\mathcal{A} + (\mathcal{B} - \mathcal{S})kL_{\text{sat}}}{1 + (kL_{\text{sat}})^2}. \quad (21)$$

We see that transport relaxation brings a stabilizing term to the growth rate when $\mathcal{A} > 0$, which dominates at large wave numbers (**Figure 5a**). Thus transport relaxation stabilizes short waves, like the slope effect.

4.2. Linear Wavelength Selection

The most unstable mode is expected to correspond to the observed wavelength emerging from an initially flat bed, at least for short times when nonlinear effects are still negligible. We discuss here the competition of the mechanisms at work for the selection of this mode, which involves a hydrodynamical length scale (the inner layer thickness δ_i or the roughness length z_0), the transport relaxation length L_{sat} , and the dimensionless slope parameter \mathcal{S} .

4.2.1. Zero L_{sat} . We first ignore the transport relaxation so that only the slope effect may counteract the destabilizing fluid inertia. The most unstable wave number is nearly proportional to the cutoff wave number k_c , which is the solution of $\mathcal{B}(k_c, z_0) = \mathcal{S}$ according to Equation 21 and can be obtained graphically from **Figure 3**. Using the asymptotic expression (Equation 8) for \mathcal{B} (laminar inertial regime), one can obtain a good estimate of the most amplified wavelength as (Charru & Mouilleron-Arnould 2002)

$$\lambda = 2\pi \frac{3\mathcal{S}}{\gamma_L} \delta_i \quad \text{or} \quad \lambda = 2\pi \left(\frac{3\mathcal{S}}{\gamma_L} \right)^{3/2} \delta_v. \quad (22)$$

The full calculation in the smooth hydrodynamical regime (**Figure 3b**) confirms this scaling with the hydrodynamical length δ_v (Sumer & Bakioglu 1984).

Using measured values of \mathcal{S} (Section 3), one finds that the predicted wavelength in water is much smaller, by one order of magnitude at least, than the measured wavelengths (**Figure 5a**). Large values of \mathcal{S} , likely unrealistic, are necessary to reduce the discrepancy [e.g., $\mathcal{S} = 2.8$ used by Richards (1980)]. For aeolian dunes, the mismatch reaches three orders of magnitude. Hence, although some uncertainties remain on the values of \mathcal{S} , the slope effect alone is not stabilizing enough.

4.2.2. Nonzero L_{sat} . **Figure 5b** displays the most unstable wavelength λ/L_{sat} as a function of L_{sat}/z_0 , calculated from Equation 21 for the three hydrodynamical models discussed in Section 2. When the saturation length is small compared to the hydrodynamical length, e.g., $L_{\text{sat}} < 10 z_0$, it appears that the selected wavelength is essentially controlled by the hydrodynamics, which is in the laminar regime. In particular, for nonzero \mathcal{S} , the scaling in Equation 22 is recovered.

For large L_{sat}/z_0 and $\mathcal{S} = 0$, **Figure 5b** shows that λ/L_{sat} is nearly constant and in the range 15–30, which means that λ scales approximately on L_{sat} . In the hydrodynamically rough regime (blue solid line), this result can be understood from the fact that for $kz_0 \ll 1$, \mathcal{A} and \mathcal{B} depend weakly—logarithmically—on kz_0 and can be considered as constants and evaluated at z_0/L_{sat} . Then the most amplified wave number is expected to scale on the cutoff wave number k_c defined by $\mathcal{B}(k_c, z_0) = \mathcal{A}(k_c, z_0)k_c L_{\text{sat}}$, i.e., the balance of destabilizing fluid inertia and stabilizing particle

relaxation. This analysis finally gives (Andreotti et al. 2002)

$$\lambda \propto \frac{\mathcal{A}(z_0/L_{\text{sat}})}{\mathcal{B}(z_0/L_{\text{sat}})} L_{\text{sat}}. \quad (23)$$

In the hydrodynamically smooth regime (curves for the smooth closure and Hanratty's model in **Figure 5b**, red and gray lines), the above scaling is recovered but at larger L_{sat}/z_0 ($>10^4$), i.e., in the turbulent regime. For smaller L_{sat}/z_0 in the range 10^1 – 10^4 , i.e., in the more complicated transitional regime (green area), the selected wavelength depends on both z_0 and L_{sat} .

The slope effect parameterized by S induces a further stabilizing effect, which results in larger wavelengths (dashed lines in **Figure 5b**). When $S > \mathcal{B}(kz_0)$ for all wave numbers, the flat bed is stable (at the right of the dots ending the dashed lines). This situation is more likely to happen close to the transport threshold at which the slope effect is stronger, and in the turbulent regime in which \mathcal{B} decreases below $S = 1.6$. Further from threshold, S decreases and long waves become unstable.

4.2.3. Aeolian dunes. The best understood situation is that of aeolian dunes, for which wind-tunnel experiments have provided measurements of q_{sat} , L_{sat} , S , and z_0 (e.g., Andreotti et al. 2010, Creyssels et al. 2009, Ho et al. 2011, Iversen & Rasmussen 1999). Aeolian transport takes place in the turbulent regime for which hydrodynamical calculations are robust with respect to turbulent closures and lead to nearly constant \mathcal{A} and \mathcal{B} (**Figure 3**). Moreover, the different lengths of the problem are well separated (**Table 1**). **Figure 6c** displays the development of dunes on the flank of large barchans (Elbelrhiti et al. 2005). In this situation, L_{sat} is the relevant length scale, and Equation 23 holds. With the slope effect, Equation 23 becomes $\lambda \propto \frac{\mathcal{A}}{\mathcal{B}-S} L_{\text{sat}}$, which predicts an increase of λ close to the transport threshold, in agreement with observations (**Figure 6d**) (Andreotti et al. 2010).

One may assess the proportionality of the saturation length with the drag length $(\rho_p/\rho_f)d$ (**Figure 4b**) by comparing dune sizes in different environments. In particular, the proportionality explains why on Mars, where the atmosphere is significantly lighter than on Earth, dunes have wavelengths ten times larger than those on Earth (Claudin & Andreotti 2006). Conversely, aeolian features that emerge under high-pressure CO_2 are on the decimeter scale (Greeley et al. 1984). As for the growth rate $\sigma \sim L_{\text{sat}}^2/Q$, its dependence on L_{sat}^2 may explain the apparent large-scale inactivity of Martian dunes, as it predicts a very large growth time, typically centuries, in contrast to days on Earth. Recent observations of the propagation of small ripples confirm that Mars is active (Silvestro et al. 2010).

4.2.4. Subaqueous ripples. The situation in liquids is less definite than in air for the following reasons: (a) The separation of the length scales, δ_i , L_{sat} , z_0 , and δ_i , is less pronounced (**Table 1**); (b) no direct measurement of L_{sat} is available yet; and (c) the observed ripples lie at the transition between the laminar and turbulent regimes, which is more sensitive to flow modeling (**Figure 6b**). Numerous experiments have been performed with various particles, with a free surface or an upper wall, but a rather limited range of the parameters has been explored (e.g., the grain Reynolds number d/δ_v and the distance to threshold u_*/u_{th}). Moreover, the focus is often on mature ripples rather than on the first stages of the instability.

Initial ripple wavelengths are typically in the range 100 – $800d$ both in water (Baas 1994, 1999; Betat et al. 1999; Coleman & Melville 1996; Fourrière et al. 2010; Langlois & Valance 2007) and in viscous fluids (Charru & Mouilleron-Arnould 2002, Kuru et al. 1995). **Figure 5a** displays measured growth rates and a fit with Equation 21 including both the slope effect and a (somewhat large) saturation length. **Figure 6b** displays measured wavelengths from the above references

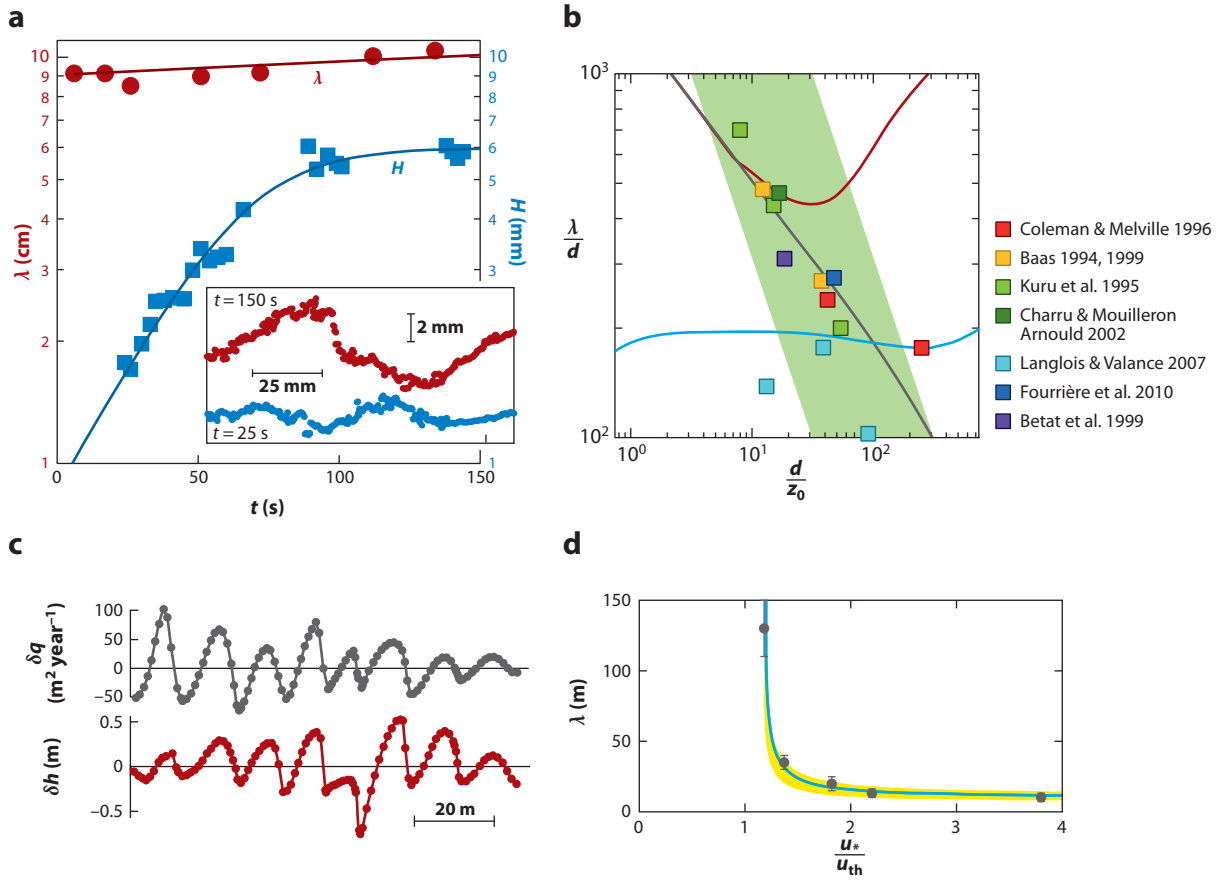


Figure 6

(a) Time evolution of the amplitude H (blue squares) and wavelength λ (red circles) of ripples in a natural river in Gascogne from a flat sand bed. (Inset) Bed profiles at $t = 25$ s and $t = 150$ s. (b) Measured initial wavelengths λ/d as a function of d/z_0 for u^*/u_{th} in the range 1.8 ± 0.2 . The solid lines are predictions for the most unstable wavelength, with $S = 0.5$ and $L_{sat}/d = 2.5 U(d)/V_{fall}$ (rough case) and $12 U(d)/V_{fall}$ (smooth case). The lines are color coded as follows: smooth closure (Equation 3) (solid red line), Hanratty's model (solid gray line), and rough closure (Equation 4) (solid blue line). The green region is the transition between the laminar and turbulent regimes ($10^{-5} < k z_0 < 10^{-3}$). (c) Profile δh of dunes on the flank of a large barchan and corresponding sand flux perturbation δq . (d) The measured initial wavelength of aeolian dunes as a function of the rescaled wind velocity. The yellow region represents the uncertainty on the value of L_{sat} in the range 0.5–0.9 m.

together with the most amplified mode computed from the three hydrodynamical models. It can be seen that subaqueous ripples form in the transitional regime in which the most amplified wavelength involves both L_{sat} and δ_v . The general trend that emerges is the decrease of λ/d with d/δ_v . Only Hanratty's model reproduces the correct trend, with the saturation length fitted to $L_{sat} \simeq 12 \frac{U}{V_{fall}} d$, consistent with measurements of the deposition length by Lajeunesse et al. (2010).

The existence of an instability threshold larger than the transport threshold is consistent with the observation of a lower-plane regime reported in bed-form stability diagrams (Southard 1991). An upper-plane regime in which the bed forms flatten and disappear is also reported in these diagrams, which generally corresponds to large particle Reynolds number, typically $d/\delta_v > 25$. Sumer & Bakioglu (1984) account for this observation with a shift of the mixing length depending

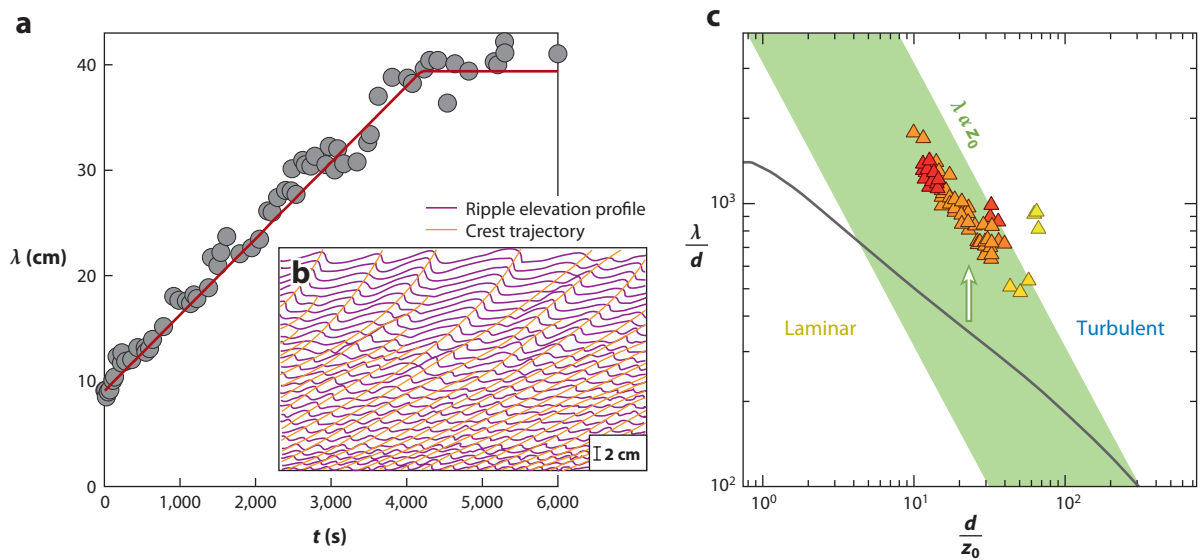


Figure 7

(a) Slow time evolution of the wavelength by pattern coarsening after the initial stage shown in **Figure 6a** and saturation due to the influence of the river depth. (b) Spatiotemporal diagram of the nonlinear coarsening (Coleman & Melville 1994). (c) Wavelengths collected by Yalin (1985) for final subaqueous ripples (triangles), for $u_*/u_{th} < 1.5$, in the graph λ/d versus d/z_0 . The symbol colors code for the grain diameter, which goes from 105 (red) to 260 μm (yellow). The arrow shows that these values are reached at the end of the pattern coarsening. It indicates the increase of the wavelength in the course of time, starting from the gray line of **Figure 6b** (Hanratty's model), which is shown for reference. Most of the ripple lengths reported in the literature correspond to mature nonlinear bed forms (Guy et al. 1966, Yalin 1985) not linear waves. A selection of these measurements close to threshold ($u_* < 1.5 u_{th}$) is displayed in **Figure 6d**. Interestingly, they fall on nearly a straight line close to the edge of the transitional regime (the left edge in **Figure 3**), $k\delta_v \approx 3 \times 10^{-4}$.

on the roughness. Another explanation could be that for large grains, the flow depth is relatively smaller, or that the transport layer thickens and the saturation length becomes larger, whose effects are stabilizing (Section 5).

4.3. Nonlinear Coarsening

We now turn to nonlinear aspects, restricting the discussion to subaqueous ripples. Once the quasi-sinusoidal ripples have emerged from the flat bed, their height $H = 2\zeta_0$ first grows exponentially with time (**Figure 7a**) (Betat et al. 1999, Fourrière et al. 2010). Then nonlinear effects quickly arise: The profile becomes asymmetrical (inset in **Figure 7a**), and after a couple of minutes the ripple height saturates, while the wavelength remains unchanged. Then, on a much longer timescale (hours), the small velocity differences related to small height differences ($c \propto 1/H$; Section 1) lead to collisions and merging between adjacent ripples (see the spatiotemporal diagram in the inset of **Figure 7b**) (Betat et al. 2002, Coleman & Melville 1994). This results in coarsening of the pattern and an increase of the averaged wavelength (**Figure 7a**). Eventually, λ saturates because of finite-size effects (see Section 5).

5. FINITE-SIZE EFFECTS

We now consider bounded flow, i.e., $kD \lesssim 1$, for which the upper boundary, either a rigid wall (closed channels) or a free surface (open channels, rivers, stratified atmosphere), is expected to

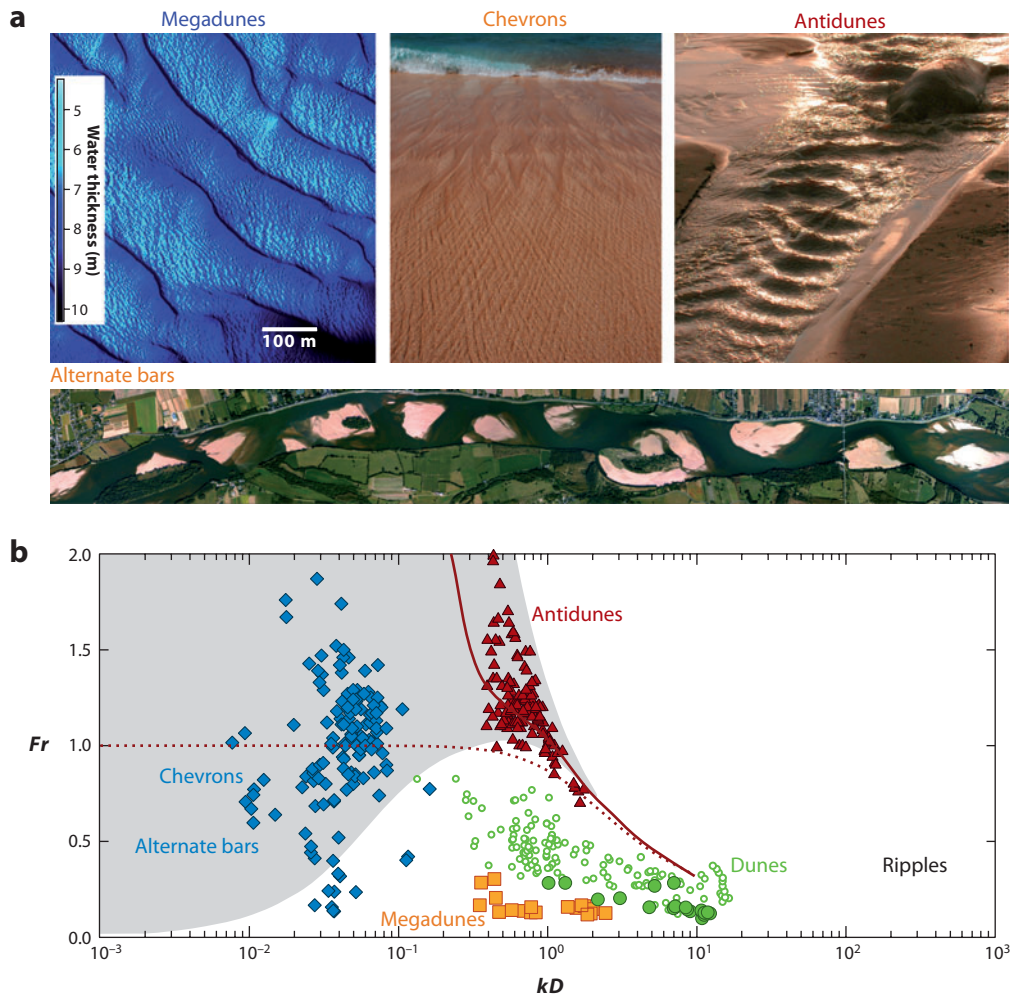


Figure 8

(a) Photographs of bed forms with $kD \lesssim 1$ (finite-depth or finite-width effects). (b) Data set of bed forms in the plane (kD, Fr) , from measurements in the natural environment as well as in flume experiments. The different bed form types are located in different regions of the diagram. $B < 0$ (gray region), and $B > 0$ (white region). For the data references, readers are referred to Andreotti et al. (2012).

affect the bottom shear stress. Several new patterns arise, such as subaqueous dunes, antidunes, chevrons, and alternate bars (Figure 8a).

5.1. Hydrodynamics

For a rigid upper boundary, the only new parameter is kD . As this parameter decreases, the inner layer progressively invades the whole flow. The sole effect of the confinement is to lower inertia so that the in-quadrature shear-stress component B decreases for both laminar and turbulent flows (Charru & Mouilleron-Arnould 2002, Engelund 1970, Fourrière et al. 2010, Richards 1980).

For a free surface flow with surface velocity U , an additional parameter enters the analysis: the Froude number $Fr = U / \sqrt{gD}$, which measures the relative magnitude of inertia and gravity. The situation can be summarized as follows. For subcritical flow ($Fr < 1$), the confinement is

Subaqueous dune:

large bed form whose size scales on the water depth

Antidune:

subaqueous bed form propagating upstream in supercritical flow

still stabilizing: The in-phase shear-stress component \mathcal{A} increases, whereas \mathcal{B} decreases and even becomes negative for $kD \ll 1$. The Saint-Venant equations, for instance, produce a negative \mathcal{B} (Gradowczyk 1968, Luchini & Charru 2010). For the more general case of three-dimensional flow over a wavy bottom $\zeta = \zeta_0 \cos(k_x x) \cos(k_y y)$, only the component \mathcal{B}_x parallel to the main flow becomes negative, whereas the transverse component \mathcal{B}_y is enhanced (Andreotti et al. 2012). For supercritical flow ($Fr > 1$), the free surface is crucial when the surface waves resonate with the undulations of the bottom, which occurs in a narrow window in the diagram (Fr, kD) (Engelund 1970). The resonance induces a sharp decrease of \mathcal{B} and also strongly affects \mathcal{A} , which can become negative.

5.2. Linear Instability and Pattern Formation

Linear stability analysis can be performed as above, with \mathcal{A} and \mathcal{B} now encoding the finite- D effect. Sediment transport remains unchanged and essentially imposes the length scale L_{sat} . Different regimes are found, depending on the dimensionless ratio L_{sat}/D (Andreotti et al. 2012). For small L_{sat}/D and $Fr < 1$, the most unstable wavelength is not influenced by the free surface and remains as in the unbounded case (ripples). In particular, there is no secondary maximum to be associated with dunes. Experimental evidence (see **Figure 7**) strongly suggests that dunes emerge from the pattern coarsening of ripples (Coleman & Melville 1994, Fourrière et al. 2010, Raudkivi 2006, Raudkivi & Witte 1990) rather than by linear instability (Colombini 2004, McLean 1990, Richards 1980). The increase of the mean wavelength is stopped by the stabilizing role of the free surface at small kD , and λ eventually scales with D . In the aeolian case, the stratified structure of the atmosphere above deserts is qualitatively analogous to a river surrounded by air: The equivalent of the flow depth is the thickness of the convective boundary layer, capped by the thin inversion layer, which plays the role of the free surface. This stratification, with thickness varying by a factor of up to 5 from coastal to continental deserts, bounds the size of giant aeolian dunes (Andreotti et al. 2009).

For $L_{\text{sat}}/D \gtrsim 0.1$ and still subcritical flow, oblique bed forms with angle α with the flow direction are more unstable than transverse ones ($\alpha = 0$). This explains the generation, in shallow water, of rhomboid beach patterns or chevrons (the combination of two plane waves with angles α and $-\alpha$) (Daerr et al. 2003, Devauchelle et al. 2010, Morton 1978, Venditti et al. 2005). This also explains the oblique or alternate bars observed in flumes with coarse grains (Lanzoni 2000, Lisle et al. 1991). Large values of L_{sat}/D are also reached when suspension is the dominant mode of transport (Section 3). Some alternate bars observed in flume experiments are in this regime (Chang et al. 1971), as well as the bars formed in rivers during floods, in which most of the sediment is suspended. In rivers and flumes, the depth-to-width ratio D/W is a new control parameter, with the transverse wave number of bed forms being selected by the finite width. The braiding patterns observed for small D/W can be interpreted as high-order modes.

For supercritical Froude number ($Fr > 1$), the free surface now has a destabilizing effect associated with the change of sign of \mathcal{A} at the resonance. The growth rate of modes with $kD \simeq 1$ dominates that of ripples when $L_{\text{sat}} \gtrsim D$. This situation corresponds to large deformations of the free surface and antidunes propagating upstream (Kennedy 1969, Parker 1975). The range of unstable wave numbers kD is so closely related to the resonance, and thus so narrow, that the most unstable mode is selected by the hydrodynamics, $\lambda \propto D$. Moreover, antidunes hardly experience pattern coarsening.

Measured wavelengths corresponding to the patterns described above are displayed in the (Fr, kD) diagram of **Figure 8**. They gather in different groups. Antidunes nicely follow the resonant curve (red solid line), whereas dunes (and megadunes) lie in the subcritical unstable region.

Chevrons:

subaqueous inclined (nontransverse) bed forms emerging in shallow flows

Alternate bars:

nontransverse features forming in rivers and flumes, with a size much larger than the flow depth

SUMMARY POINTS

1. The formation of subaqueous ripples and aeolian dunes in unbounded flow (bed-form wavelength smaller than the flow depth) results from the destabilizing action of fluid inertia, which induces a phase advance of the shear stress relative to the bed disturbance.
2. The most relevant hydrodynamical length is the thickness δ_i of the inner layer above which the dynamics of the flow disturbance is essentially inviscid and potential.
3. The destabilizing inertia is balanced by the stabilizing lag of the particle flux with respect to shear stress. The saturation length L_{sat} associated with this relaxation effect is an essential feature for our understanding of the instability. A second stabilizing effect is the bed-form slope, which drags the particles toward troughs.
4. For aeolian dunes, the scales of the problem are well separated; the initial dune wavelength is, as a first approximation, proportional to the saturation length times the hydrodynamical factor \mathcal{B}/\mathcal{A} encoding the phase advance of the bed shear stress. The saturation length results from grain inertia and is proportional to the drag length $(\rho_p/\rho_f)d$. Weaker effects arise from the dependence of λ/L_{sat} to L_{sat}/z_0 and the slope parameter \mathcal{S} .
5. For subaqueous ripples, the conclusion is less clear-cut. Most experimental and field data lie in the transition between the laminar and turbulent regimes, in which the bed shear stress is more sensitive to turbulence modeling. However, there is direct evidence that ripples form by the linear instability of a flat bed, and their initial wavelength, in the range $100\text{--}800d$, is consistent with L_{sat} in the range $10\text{--}30d$. The rapid coarsening of the pattern makes the interpretation of many data from the literature difficult.

FUTURE ISSUES

1. The laminar-turbulent transitional regime, in which most of the subaqueous ripples lie, remains to be understood. The effect on the bed shear stress of turbulent coherent structures in the near-bed region, notably longitudinal streaks, is largely unknown.
2. The nonlinear description of the hydrodynamical response to a complex relief remains to be completed, in particular, the secondary flows behind star dunes and other three-dimensional dunes.
3. The saturation length L_{sat} for bed load has to be measured and understood, as well as its large increase at the transition from bed load to suspension.
4. A quantitative nonlinear description of the asymmetry and saturated amplitude of dunes is open, as well as the description of dune interactions, collisions, coalescence, and splitting, in one-dimensional channels and two-dimensional fields.
5. Finally, the effects of grain polydispersity and segregation have to be understood.

DISCLOSURE STATEMENT

The authors are not aware of any biases that might be perceived as affecting the objectivity of this review.

ACKNOWLEDGMENTS

This work has benefited from the financial support of the Agence Nationale de la Recherche, grant “Zephyr” (ERCS07_18) and from that of the Groupement de Recherche MéPhy (CNRS GDR 3166). Some of the field data presented here have been obtained in agreement with the Parc Naturel Régional des Landes de Gascogne.

LITERATURE CITED

- Abrams J, Hanratty TJ. 1985. Relaxation effects observed for turbulent flow over a wavy surface. *J. Fluid Mech.* 151:443–55
- Anderson RS, Haff PK. 1988. Simulation of aeolian saltation. *Science* 241:820–23
- Andreotti B. 2004. A two species model of aeolian sand transport. *J. Fluid Mech.* 510:47–50
- Andreotti B, Claudin P, Devauchelle O, Durán O, Fourrière A. 2012. Bedforms in a turbulent stream: ripples, chevrons and antidunes. *J. Fluid Mech.* 690:94–128
- Andreotti B, Claudin P, Douady S. 2002. Selection of dune shapes and velocities. Part 2: A two-dimensional modelling. *Eur. Phys. J. B* 28:341–52
- Andreotti B, Claudin P, Pouliquen O. 2010. Measurements of the aeolian sand transport saturation length. *Geomorphology* 123:343–48
- Andreotti B, Fourrière A, Ould-Kaddour F, Murray AB, Claudin P. 2009. Giant aeolian dune size determined by the averaged depth of the atmospheric boundary layer. *Nature* 457:1120–23
- Ashida K, Okabe T. 1982. On the calculation method of the concentration of suspended sediment under non-equilibrium condition. *Proc. 26th Conf. Hydraul.*, pp. 153–58. Tokyo: Jpn. Soc. Civil Eng. (In Japanese)
- Ayotte KW, Xu D, Taylor PA. 1994. The impact of turbulence closure schemes on predictions of the mixed spectral finite-difference model for flow over topography. *Bound.-Layer Meteorol.* 68:1–33
- Baas JH. 1994. A flume study on the development and equilibrium morphology of current ripples in very fine sand. *Sedimentology* 41:185–209
- Baas JH. 1999. An empirical model for the development and the equilibrium morphology of current ripples in fine sand. *Sedimentology* 46:123–38
- Baddock MC, Livingstone I, Wiggs GFS. 2007. The geomorphological significance of airflow patterns in transverse dune interdunes. *Geomorphology* 87:322–36
- Bagnold RA. 1941. *The Physics of Blown Sand and Desert Dunes*. London: Methuen
- Bagnold RA. 1956. The flow of cohesionless grains in fluids. *Philos. Trans. R. Soc. Lond. A* 249:235–97
- Belcher SE, Hunt JCR. 1998. Turbulent flow over hills and waves. *Annu. Rev. Fluid Mech.* 30:507–38
- Benjamin TB. 1959. Shearing flow over a wavy boundary. *J. Fluid Mech.* 6:161–205
- Best J. 2005. The fluid dynamics of river dunes: a review and some future research directions. *J. Geophys. Res.* 110:F04S02
- Betat A, Frette V, Rehberg I. 1999. Sand ripples induced by water shear flow in an annular channel. *Phys. Rev. Lett.* 83:88–91
- Betat A, Krüille CA, Frette V, Rehberg I. 2002. Long-time behavior of sand ripples induced by water shear flow. *Eur. Phys. J. E* 8:465–76
- Blondeaux P. 1990. Sand ripples under sea waves. Part 1. Ripple formation. *J. Fluid Mech.* 218:1–17
- Blondeaux P. 2001. Mechanics of coastal forms. *Annu. Rev. Fluid Mech.* 33:339–70
- Bordner GL. 1978. Nonlinear analysis of laminar boundary layer flow over a periodic wavy surface. *Phys. Fluids* 21:1471–64
- Bourke MC, Lancaster N, Fenton LK, Parteli EJR, Zimbelman JR, Radebaugh J. 2010. Extraterrestrial dunes: an introduction to the special issue on planetary dune systems. *Geomorphology* 121:1–14
- Buckles J, Hanratty TJ, Adrian RJ. 1984. Turbulent flow over large-amplitude wavy surfaces. *J. Fluid Mech.* 140:27–44
- Caponi EA, Fornberg B, Kight DD, McLean JW, Saffman PG, Yuen HC. 1982. Calculations of laminar viscous flow over a moving wavy surface. *J. Fluid Mech.* 124:247–62
- Chang HY, Simons DB, Woolhiser DA. 1971. Flume experiments on alternate bar formation. *J. Waterw. Harb. Coast. Eng. Div.* 97:155–65

- Charru F. 2006. Selection of the ripple length on a granular bed sheared by a liquid flow. *Phys. Fluids* 18:121508
- Charru F, Hinch EJ. 2000. 'Phase diagram' of interfacial instabilities in a two-layer Couette flow and mechanism for the long-wave instability. *J. Fluid Mech.* 414:195–223
- Charru F, Hinch EJ. 2006a. Ripple formation on a particle bed sheared by a viscous liquid. Part 1. Steady flow. *J. Fluid Mech.* 550:111–21
- Charru F, Hinch EJ. 2006b. Ripple formation on a particle bed sheared by a viscous liquid. Part 2. Oscillating flow. *J. Fluid Mech.* 550:123–37
- Charru F, Mouilleron-Arnould H. 2002. Instability of a bed of particles sheared by a viscous flow. *J. Fluid Mech.* 452:303–23
- Charru F, Mouilleron H, Eiff O. 2004. Erosion and deposition of particles on a bed sheared by a viscous flow. *J. Fluid Mech.* 519:55–80
- Cherukat P, Na Y, Hanratty TJ, McLaughlin JB. 1998. Direct numerical simulation of a fully developed turbulent flow over a wavy wall. *Theoret. Comput. Fluid Dyn.* 11:109–34
- Claudin P, Andreotti B. 2006. A scaling law for aeolian dunes on Mars, Venus, Earth, and for sub-aqueous ripples. *Earth Planet. Sci. Lett.* 252:30–44
- Claudin P, Charru F, Andreotti B. 2011. Transport relaxation time and length scales in turbulent suspensions. *J. Fluid Mech.* 671:491–506
- Claudin P, Wiggs GFS, Andreotti B. 2012. Field evidence for the upwind velocity shift at the crest of low dunes. *Bound.-Layer Meteorol.* Manuscript submitted. arXiv: 1205.4411
- Coleman SE, Melville BW. 1994. Bed-form development. *J. Hydraul. Eng.* 120:544–60
- Coleman SE, Melville BW. 1996. Initiation of bed forms on a flat sand bed. *J. Hydraul. Eng.* 122:301–10
- Colombini M. 2004. Revisiting the linear theory of sand dune formation. *J. Fluid Mech.* 502:1–16
- Colombini M, Stocchino A. 2008. Finite-amplitude river dunes. *J. Fluid Mech.* 611:283–306
- Creysseels M, Dupont P, Ould el Moutar A, Valance A, Cantat I, et al. 2009. Saltating particles in a turbulent boundary layer: experiment and theory. *J. Fluid Mech.* 625:47–74
- Daerr A, Lee P, Lanuza J, Clément E. 2003. Erosion patterns in a sediment layer. *Phys. Rev. E* 67:065201
- de Angelis V, Lombardi P, Banerjee S. 1997. Direct numerical simulation of turbulent flow over a wavy wall. *Phys. Fluids* 9:2429–42
- Devauchelle O, Malverti L, Lajeunesse E, Josserand C, Lagrée P-Y, Métivier F. 2010. Rhomboid beach pattern: a laboratory investigation. *J. Geophys. Res.* 115:F02017
- Dey S. 2003. Threshold of sediment motion on combined transverse and longitudinal sloping beds. *J. Hydraul. Res.* 41:405–15
- Durán O, Claudin P, Andreotti B. 2011. On aeolian transport: grain-scale interactions, dynamical mechanisms and scaling laws. *Aeolian Res.* 3:243–70
- Elbelrhiti H, Claudin C, Andreotti B. 2005. Field evidence for surface wave induced instability of sand dunes. *Nature* 437:720–23
- Engelund F. 1970. Instability of erodible beds. *J. Fluid Mech.* 42:225–44
- Engelund F, Fredsøe J. 1982. Sediment ripples and dunes. *Annu. Rev. Fluid Mech.* 14:13–37
- Fernandez Luque R, van Beek R. 1976. Erosion and transport of bed-load sediment. *J. Hydraul. Res.* 14:127–44
- Finnigan JJ, Raupach MR, Bradley EF, Aldis GK. 1990. A wind tunnel study of turbulent flow over a two-dimensional ridge. *Bound.-Layer Meteorol.* 50:277–317
- Fourrière A, Claudin P, Andreotti B. 2010. Bedforms in a turbulent stream: formation of ripples by primary linear instability and of dunes by non-linear pattern coarsening. *J. Fluid Mech.* 649:287–328
- Frederick KA, Hanratty TJ. 1988. Velocity measurements for a turbulent nonseparated flow over solid waves. *Exp. Fluids* 6:477–86
- Fredsøe J. 1974. On the development of dunes in erodible channels. *J. Fluid Mech.* 64:1–16
- Fryberger SG, Dean G. 1979. Dune forms and wind regime. In *A Study of Global Sand Seas*, ed. ED McKee, pp. 137–69. US Geol. Surv. Prof. Pap. 1052. Washington, DC: US Geol. Surv.
- Gong W, Ibbetson A. 1989. A wind tunnel study of turbulent flow over model hills. *Bound.-Layer Meteorol.* 49:113–48
- Gong W, Taylor PA, Dörnbrack A. 1996. Turbulent boundary-layer flow over fixed aerodynamically rough two-dimensional sinusoidal waves. *J. Fluid Mech.* 312:1–37

- Gradowczyk MH. 1968. Wave propagation and boundary instability in erodible-bed channels. *J. Fluid Mech.* 33:93–112
- Greeley R, Marshall JR, Leach RN. 1984. Microdunes and other aeolian bedforms on Venus: wind tunnel simulations. *Icarus* 60:152–60
- Guy H, Simons D, Richardson E. 1966. *Summary of Alluvial Channel Data from Flume Experiments, 1956–61*. US Geol. Surv. Prof. Pap. 462-I. Washington, DC: US Geol. Surv.
- Henn DS, Sykes RI. 1999. Large-eddy simulation of slow over wavy surfaces. *J. Fluid Mech.* 383:75–112
- Hersen P, Douady S, Andreotti B. 2002. Relevant lengthscale of barchan dunes. *Phys. Rev. Lett.* 89:264301
- Ho TD, Valance A, Dupont P, Ould El Moctar A. 2011. Scaling laws in aeolian sand transport. *Phys. Rev. Lett.* 106:094501
- Hudson JD, Dykhno L, Hanratty TJ. 1996. Turbulence production in flow over a wavy wall. *Exp. Fluids* 20:257–65
- Hunt JCR, Leibovich S, Richards KJ. 1988. Turbulent shear flows over low hills. *Q. J. R. Meteorol. Soc.* 114:1435–70
- Iversen JD, Rasmussen KR. 1999. The effect of wind speed and bed slope on sand transport. *Sedimentology* 46:723–31
- Jackson PS, Hunt JCR. 1975. Turbulent wind flow over a low hill. *Q. J. R. Meteorol. Soc.* 101:929–55
- Jensen N-O, Zeman O. 1985. Perturbations to mean wind turbulence in flow over topographic forms. In *International Workshop on the Physics of Blown Sand*, ed. OE Barndor-Nielsen, K Møller, KR Rasmussen, BB Willets, pp. 351–68. Aarhus, Den.: Univ. Aarhus
- Jobson AE, Sayre WW. 1970. Vertical transfer in open channel flow. *J. Hydraul. Div. ASCE* 96:703–24
- Kamphuis JW. 1974. Determination of sand roughness for fixed beds. *J. Hydraul. Res.* 12:193–207
- Kennedy JF. 1963. The mechanics of dunes and antidunes in erodible bed channels. *J. Fluid Mech.* 16:521–44
- Kennedy JF. 1969. The formation of sediment ripples, dunes and antidunes. *Annu. Rev. Fluid Mech.* 1:147–68
- Kroy K, Sauermann G, Herrmann HJ. 2002. Minimal model for aeolian sand dunes. *Phys. Rev. E* 66:031302
- Kruse N, Günther Q, Rudolf von Rohr P. 2003. Dynamics of large-scale structures in turbulent flow over a wavy wall. *J. Fluid Mech.* 485:87–96
- Kuru WC, Leighton DT, McCready MJ. 1995. Formation of waves on a horizontal erodible bed of particles. *Int. J. Multiphase Flow* 21:1123–40
- Kuzan JD, Hanratty TJ, Adrian RJ. 1989. Turbulent flows with incipient separation over solid waves. *Exp. Fluids* 7:88–98
- Lagrée P-Y. 2003. A triple deck model of ripple formation and evolution. *Phys. Fluids* 15:2355–68
- Lajeunesse E, Malverti L, Charru F. 2010. Bedload transport in turbulent flow at the grain scale: experiments and modeling. *J. Geophys. Res.* 115:F04001
- Langlois V, Valance A. 2007. Formation and evolution of current ripples on a flat sand bed under turbulent water flow. *Eur. Phys. J. E* 22:201–8
- Lanzoni S. 2000. Experiments on bar formation in a straight flume. 2. Uniform sediment. *Water Resour. Res.* 36:3351–63
- Leighton D, Acrivos A. 1986. Viscous resuspension. *Chem. Eng. Sci.* 41:1377–84
- Lisle TE, Ikeda H, Iseya F. 1991. Formation of stationary alternate bars in a steep channel with mixed-size sediment: a flume experiment. *Earth Surf. Process. Landf.* 16:463–69
- Loiseleux T, Gondret P, Rabaud M, Doppler D. 2005. Onset of erosion and avalanche for an inclined granular bed sheared by a continuous laminar flow. *Phys. Fluids* 17:103304
- Luchini P, Charru F. 2010. The phase lead of shear stress in shallow-water flow over a perturbed bottom. *J. Fluid Mech.* 665:516–39
- Mason PJ, King JC. 1985. Measurements and predictions of flow and turbulence over an isolated hill of moderate slope. *Q. J. R. Meteorol. Soc.* 111:617–40
- McLean SR. 1990. The stability of ripples and dunes. *Earth-Sci. Rev.* 29:131–44
- Morton RA. 1978. Large-scale rhomboid bed forms and sedimentary structures associated with hurricane washover. *Sedimentology* 25:183–204
- Mouilleron H, Charru F, Eiff O. 2009. Inside the moving layer of a sheared granular bed. *J. Fluid Mech.* 628:229–39

- Narteau C, Zhang D, Rozier O, Claudin P. 2009. Setting the length and time scales of a cellular automaton dune model from the analysis of superimposed bedforms. *J. Geophys. Res.* 114:F03006
- Ouriemi M, Aussillous P, Guazzelli E. 2009. Sediment dynamics. Part 1. Bed-load transport by laminar shearing flows. *J. Fluid Mech.* 636:321–36
- Owen PR. 1964. Saltation of uniform grains in air. *J. Fluid Mech.* 20:225–42
- Parker G. 1975. Sediment inertia as cause of river anti-dunes. *J. Hydraul. Div. ASCE* 101:211–21
- Parteli EJR, Schwämmle V, Herrmann HJ, Monteiro LHU, Maia LP. 2006. Profile measurement and simulation of a transverse dune field in the Lençóis Maranhenses. *Geomorphology* 81:29–42
- Poggi D, Katul GG, Albertson JD, Ridolfi L. 2007. An experimental investigation of turbulent flows over a hilly surface. *Phys. Fluids* 19:036601
- Pope SB. 2000. *Turbulent Flows*. Cambridge, UK: Cambridge Univ. Press
- Pye K, Tsoar H. 1990. *Aeolian Sand and Sand Dunes*. London: Unwin Hyman
- Raudkivi AJ. 2006. Transition from ripples to dunes. *J. Hydraul. Eng.* 132:1316–20
- Raudkivi AJ, Witte HH. 1990. Development of bed features. *J. Hydraul. Eng.* 116:1063–79
- Raupach MR, Antonia RA, Rajagopalan S. 1991. Rough-wall turbulent boundary layers. *Appl. Mech. Rev.* 44:1–25
- Richards KJ. 1980. The formation of ripples and dunes on an erodible bed. *J. Fluid Mech.* 99:597–618
- Richards KJ, Taylor PA. 1981. A numerical model of flow over sand waves in water of finite depth. *Geophys. J. R. Astron. Soc.* 65:103–28
- Ross AN, Arnold S, Vosper SB, Mobbs SD, Dixon N, Robins AG. 2004. A comparison of wind-tunnel experiments and numerical simulations of neutral and stratified flow over a hill. *Bound.-Layer Meteorol.* 113:427–59
- Rousseaux G, Stegner A, Wesfreid JE. 2004. Wavelength selection of rolling-grain ripples in the laboratory. *Phys. Rev. E* 69:031307
- Salveti MV, Damiani R, Beux F. 2001. Three-dimensional coarse large-eddy simulations of the flow above two-dimensional sinusoidal waves. *Int. J. Numer. Methods Fluids* 35:617–42
- Sauermann G, Kroy K, Herrmann HJ. 2001. Continuum saltation model for sand dunes. *Phys. Rev. E* 64:031305
- Schafflinger U, Acrivos A, Stibi H. 1995. An experimental study of viscous resuspension in a pressure-driven plane channel flow. *Int. J. Multiphase Flow* 21:693–704
- Seminara G. 2010. Fluvial sedimentary patterns. *Annu. Rev. Fluid Mech.* 42:43–66
- Silvestro S, Fenton LK, Vaz DA, Bridges NT, Ori GG. 2010. Ripple migration and dune activity on Mars: evidence for dynamic wind processes. *Geophys. Res. Lett.* 37:L20203
- Sleath JFA. 1976. On rolling-grain ripples. *J. Hydraul. Res.* 14:69–81
- Southard JB. 1991. Experimental determination of bed-form stability. *Annu. Rev. Earth Planet. Sci.* 19:423–55
- Stevenson P, Thorpe RB, Kennedy JE, McDermott C. 2001. The transport of particles at low loading in near-horizontal pipes by intermittent flow. *Chem. Eng. Sci.* 56:2149–59
- Sumer BM, Bakioglu M. 1984. On the formation of ripples on an erodible bed. *J. Fluid Mech.* 144:177–90
- Sykes RI. 1980. An asymptotic theory of incompressible turbulent boundary-layer flow over a small bump. *J. Fluid Mech.* 101:647–70
- Taylor PA, Mason PJ, Bradley EF. 1987. Boundary-layer flow over low hills. *Bound.-Layer Meteorol.* 39:107–32
- Ungar JE, Haff PK. 1987. Steady state saltation in air. *Sedimentology* 34:289–99
- Valance A. 2011. Nonlinear sand bedform dynamics in a viscous flow. *Phys. Rev. E* 83:036304
- Valance A, Langlois V. 2005. Ripple formation over a sand bed submitted to a laminar shear flow. *Eur. Phys. J. B* 43:283–94
- van Boxel JH, Arens AM, van Dijk PM. 1999. Aeolian processes across transverse dunes. I: Modelling the air flow. *Earth Surf. Process. Landf.* 24:255–70
- van Rijn LC. 1982. Equivalent roughness of alluvial bed. *J. Hydraul. Eng.* 108:1215–18
- van Rijn LC. 1986. Application of sediment pickup function. *J. Hydraul. Eng.* 112:867–74
- Venditti JG, Church MA, Bennett SJ. 2005. Bed form initiation from a flat sand bed. *J. Geophys. Res.* 110:F01009
- Walker IJ, Nickling WG. 2003. Simulation and measurement of surface shear stress over isolated and closely spaced transverse dunes in a wind tunnel. *Earth Surf. Process. Landf.* 28:1111–24
- Weng WS, Hunt JCR, Carruthers DJ, Warren A, Wiggs GFS, et al. 1991. Air flow and sand transport over sand dunes. *Acta Mech.* 2:1–22

- Wiggs GFS, Livingstone I, Warren A. 1996. The role of streamline curvature in sand dune dynamics: evidence from field and wind tunnel measurements. *Geomorphology* 17:29–46
- Yalin MS. 1985. On the determination of ripple geometry. *J. Hydraul. Eng.* 111:1148–55
- Yue W, Lin C-L, Patel VC. 2006. Large-eddy simulation of turbulent flow over a fixed two-dimensional dune. *J. Hydraul. Eng.* 132:643–51
- Zilker DP, Cook GW, Hanratty TJ. 1977. Influence of the amplitude of a solid wavy wall on a turbulent flow. Part 1. Non-separated flows. *J. Fluid Mech.* 82:29–51
- Zilker DP, Hanratty TJ. 1979. Influence of the amplitude of a solid wavy wall on a turbulent flow. Part 2. Separated flows. *J. Fluid Mech.* 90:257–71



Contents

Hans W. Liepmann, 1914–2009 <i>Roddam Narasimha, Anatol Roshko, and Morteza Gharib</i>	1
Philip G. Saffman <i>D.I. Pullin and D.I. Meiron</i>	19
Available Potential Energy and Exergy in Stratified Fluids <i>Rémi Tailleux</i>	35
The Fluid Dynamics of Tornadoes <i>Richard Rotunno</i>	59
Nonstandard Inkjets <i>Osman A. Basaran, Haijing Gao, and Pradeep P. Bhat</i>	85
Breaking Waves in Deep and Intermediate Waters <i>Marc Perlin, Wooyoung Choi, and Zbigang Tian</i>	115
Balance and Spontaneous Wave Generation in Geophysical Flows <i>J. Vanneste</i>	147
Wave Packets and Turbulent Jet Noise <i>Peter Jordan and Tim Colonius</i>	173
Leidenfrost Dynamics <i>David Quéré</i>	197
Ice-Sheet Dynamics <i>Christian Schoof and Ian Hewitt</i>	217
Flow in Foams and Flowing Foams <i>Sylvie Cohen-Addad, Reinhard Höbner, and Olivier Pitois</i>	241
Moving Contact Lines: Scales, Regimes, and Dynamical Transitions <i>Jacco H. Snoeijer and Bruno Andreotti</i>	269
Growth of Cloud Droplets in a Turbulent Environment <i>Wojciech W. Grabowski and Lian-Ping Wang</i>	293
The Fluid Mechanics of Cancer and Its Therapy <i>Petros Koumoutsakos, Igor Pivkin, and Florian Milde</i>	325

Analysis of Fluid Flows via Spectral Properties of the Koopman Operator <i>Igor Mezić</i>	357
The Interaction of Jets with Crossflow <i>Krishnan Mahesh</i>	379
Particle Image Velocimetry for Complex and Turbulent Flows <i>Jerry Westerweel, Gerrit E. Elsinga, and Ronald J. Adrian</i>	409
Fluid Dynamics of Human Phonation and Speech <i>Rajat Mittal, Byron D. Erath, and Michael W. Plesniak</i>	437
Sand Ripples and Dunes <i>François Charru, Bruno Andreotti, and Philippe Claudin</i>	469
The Turbulent Flows of Supercritical Fluids with Heat Transfer <i>Jung Yul Yoo</i>	495

Indexes

Cumulative Index of Contributing Authors, Volumes 1–45	527
Cumulative Index of Chapter Titles, Volumes 1–45	536

Errata

An online log of corrections to *Annual Review of Fluid Mechanics* articles may be found at <http://fluid.annualreviews.org/errata.shtml>